

# Layer-dependent ferromagnetism in a van der Waals crystal down to the monolayer limit

Bevin Huang<sup>1\*</sup>, Genevieve Clark<sup>2\*</sup>, Efrén Navarro-Moratalla<sup>3\*</sup>, Dahlia R. Klein<sup>3</sup>, Ran Cheng<sup>4</sup>, Kyle L. Seyler<sup>1</sup>, Ding Zhong<sup>1</sup>, Emma Schmidgall<sup>1</sup>, Michael A. McGuire<sup>5</sup>, David H. Cobden<sup>1</sup>, Wang Yao<sup>6</sup>, Di Xiao<sup>4</sup>, Pablo Jarillo-Herrero<sup>3</sup> & Xiaodong Xu<sup>1,2</sup>

Since the discovery of graphene<sup>1</sup>, the family of two-dimensional materials has grown, displaying a broad range of electronic properties. Recent additions include semiconductors with spin-valley coupling<sup>2</sup>, Ising superconductors<sup>3–5</sup> that can be tuned into a quantum metal<sup>6</sup>, possible Mott insulators with tunable charge-density waves<sup>7</sup>, and topological semimetals with edge transport<sup>8,9</sup>. However, no two-dimensional crystal with intrinsic magnetism has yet been discovered<sup>10–14</sup>; such a crystal would be useful in many technologies from sensing to data storage<sup>15</sup>. Theoretically, magnetic order is prohibited in the two-dimensional isotropic Heisenberg model at finite temperatures by the Mermin–Wagner theorem<sup>16</sup>. Magnetic anisotropy removes this restriction, however, and enables, for instance, the occurrence of two-dimensional Ising ferromagnetism. Here we use magneto-optical Kerr effect microscopy to demonstrate that monolayer chromium triiodide (CrI<sub>3</sub>) is an Ising ferromagnet with out-of-plane spin orientation. Its Curie temperature of 45 kelvin is only slightly lower than that of the bulk crystal, 61 kelvin, which is consistent with a weak interlayer coupling. Moreover, our studies suggest a layer-dependent magnetic phase, highlighting thickness-dependent physical properties typical of van der Waals crystals<sup>17–19</sup>. Remarkably, bilayer CrI<sub>3</sub> displays suppressed magnetization with a metamagnetic effect<sup>20</sup>, whereas in trilayer CrI<sub>3</sub> the interlayer ferromagnetism observed in the bulk crystal is restored. This work creates opportunities for studying magnetism by harnessing the unusual features of atomically thin materials, such as electrical control for realizing magnetoelectronics<sup>12</sup>, and van der Waals engineering to produce interface phenomena<sup>15</sup>.

Magnetic anisotropy is an important requirement for realizing two-dimensional (2D) magnetism. In ultrathin metallic films, whether an easy axis can originate from symmetry reduction at the interface or surface is dependent on substrate properties and interface quality<sup>21–23</sup>. In contrast, most van der Waals magnets have an intrinsic magnetocrystalline anisotropy owing to the reduced crystal symmetry of their layered structures. Several layered magnets exhibit effective 2D magnetic interactions even in their bulk crystal form<sup>24,25</sup>. This implies that it might be possible to retain a magnetic ground state in a monolayer. In addition to enabling the study of magnetism in naturally formed crystals in the true 2D limit, layered magnets provide a platform for studying the thickness dependence of magnetism in isolated single crystals where the interaction with the underlying substrate is weak. These covalently bonded van der Waals layers prevent complex magnetization reorientations induced by epitaxial lattice reconstruction and strain<sup>23</sup>. For layered materials, these advantages come at a low fabrication cost, since the micromechanical exfoliation technique is much simpler than conventional approaches requiring sputtering or sophisticated molecular beam epitaxy.

A variety of layered magnetic compounds have recently been investigated to determine whether their magnetic properties can be retained down to monolayer thickness<sup>12–14,26</sup>. Recent Raman studies suggest ferromagnetic ordering in few-layer Cr<sub>2</sub>Ge<sub>2</sub>Te<sub>6</sub> and antiferromagnetic ordering in monolayer FePS<sub>3</sub><sup>27,28</sup>. However, no evidence yet exists for ferromagnetism persisting down to the monolayer limit. One promising candidate is bulk crystalline CrI<sub>3</sub>. It shows layered Ising ferromagnetism below a Curie temperature ( $T_C$ ) of 61 K with an out-of-plane easy axis (Fig. 1a and b, Extended Data Fig. 1)<sup>10,29</sup>. Given its van der Waals nature, we expect magnetocrystalline anisotropy, which could possibly lift the Mermin–Wagner restriction to stabilize long-range ferromagnetic ordering even in a monolayer.

In our experiment, we obtained atomically thin CrI<sub>3</sub> flakes by mechanical exfoliation of bulk crystals onto oxidized silicon substrates (see Methods for CrI<sub>3</sub> crystal growth<sup>10</sup> and fabrication details). Given the reactivity of CrI<sub>3</sub> flakes, sample preparation was carried out in a glove box under an inert atmosphere. We mainly employed optical contrast based on the pixel red–green–blue (RGB) value to index the number of layers in a flake (see Methods for quantitative optical microscopy in CrI<sub>3</sub> and Extended Data Figs 2–4). Figure 1c is an optical micrograph of a typical multi-step CrI<sub>3</sub> flake on a 285-nm SiO<sub>2</sub>/Si substrate, showing regions ranging from 1 to 6 layers in thickness. Figure 1d shows an optical contrast map of the same region illuminated by 631-nm-filtered light. The extracted optical contrast as a function of layer thickness is in good agreement with models based on the Fresnel equations (Fig. 1e). To accurately determine the correspondence between optical contrast and flake thickness, we also measured the thickness of CrI<sub>3</sub> flakes by atomic force microscopy, determined to be 0.7 nm per layer, after encapsulation with few-layer graphene (see Extended Data Fig. 5).

To probe the magnetic order, we employed polar magneto-optical Kerr effect (MOKE) measurements as a function of applied external magnetic field perpendicular to the sample plane (Faraday geometry). This design is sensitive to out-of-plane magnetization, and can detect small Kerr rotations,  $\theta_K$ , of linearly polarized light down to 100  $\mu$ rad using an alternating-current polarization modulation technique as laid out in Extended Data Fig. 6. All optical measurements were carried out using a 633-nm HeNe laser and at a temperature of 15 K, unless otherwise specified. Figure 1f illustrates the MOKE signal from a thin bulk flake of CrI<sub>3</sub>. The observed hysteresis curve and remanent  $\theta_K$  at zero magnetic field  $\mu_0 H = 0$  T (where  $\mu_0$  is the magnetic constant) are hallmarks of ferromagnetic ordering, consistent with its bulk ferromagnetism with out-of-plane magnetization. The negative remanent  $\theta_K$  when approaching zero field from a positive external field is a consequence of thin-film interference from reflections at the CrI<sub>3</sub>–SiO<sub>2</sub> and SiO<sub>2</sub>–Si interfaces (see Methods for thin-film interference and Extended Data Fig. 7).

<sup>1</sup>Department of Physics, University of Washington, Seattle, Washington 98195, USA. <sup>2</sup>Department of Materials Science and Engineering, University of Washington, Seattle, Washington 98195, USA.

<sup>3</sup>Department of Physics, Massachusetts Institute of Technology, Cambridge, Massachusetts 02139, USA. <sup>4</sup>Department of Physics, Carnegie Mellon University, Pittsburgh, Pennsylvania 15213, USA.

<sup>5</sup>Materials Science and Technology Division, Oak Ridge National Laboratory, Oak Ridge, Tennessee 37831, USA. <sup>6</sup>Department of Physics and Center of Theoretical and Computational Physics, University of Hong Kong, Hong Kong, China.

\*These authors contributed equally to this work.

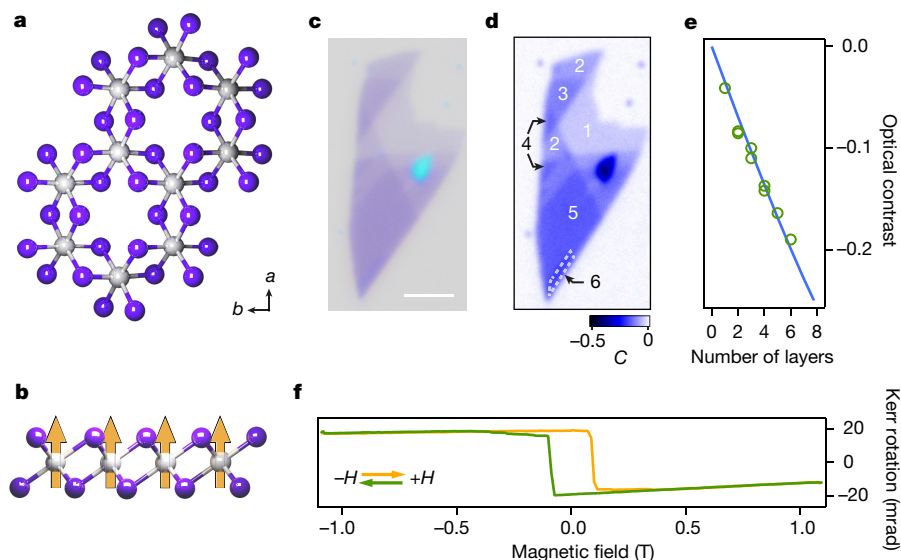


**Figure 1 | Crystal structure, layer thickness identification, and MOKE of bulk CrI<sub>3</sub>.** **a**, View of the in-plane atomic lattice of a single CrI<sub>3</sub> layer. Grey and purple balls represent Cr and I atoms, respectively. The Cr<sup>3+</sup> ions are coordinated to six I<sup>-</sup> ions to form edge-sharing octahedra arranged in a hexagonal honeycomb lattice. **b**, Out-of-plane view of the same CrI<sub>3</sub> structure depicting the Ising spin orientation. **c**, Optical micrograph of a

representative CrI<sub>3</sub> flake. **d**, Calculated optical contrast map of the same flake with a 631-nm optical filter. The scale bar in **c** is 3  $\mu\text{m}$ . **e**, Averaged optical contrast of the steps of the sample with different numbers of layers (circles) fitted by a model based on Fresnel's equations (solid line). **f**, Polar MOKE signal of a thin bulk CrI<sub>3</sub> crystal.

Remarkably, the ferromagnetic ordering remains in the monolayer limit. Figure 2a shows  $\theta_K$  as a function of  $\mu_0 H$  for a monolayer CrI<sub>3</sub> flake (inset to Fig. 2a). A single hysteresis loop in  $\theta_K$  centred around  $\mu_0 H = 0$  T, with a non-zero remanent Kerr rotation, demonstrates out-of-plane spin polarization. This implies Ising ferromagnetism in monolayer CrI<sub>3</sub>. As expected,  $\theta_K$  is independent of the excitation power (Fig. 2b). In the following, all data are taken with an excitation power of 10  $\mu\text{W}$ . We have measured a total of 12 monolayer samples, which

show similar MOKE behaviour with consistent remanent  $\theta_K$  values of about  $5 \pm 2$  mrad at  $\mu_0 H = 0$  T (Extended Data Fig. 8a). The coercive field ( $\mu_0 H_c$ ), which is approximately 50 mT for the sample in Fig. 2a, can vary between samples owing to the formation of domain structures in some samples.

Figure 2c shows spatial maps of  $\theta_K$  for another monolayer, taken at selected magnetic field values. After cooling the sample from above  $T_C$  at  $\mu_0 H = 0$  T, the entire monolayer is spontaneously magnetized (in

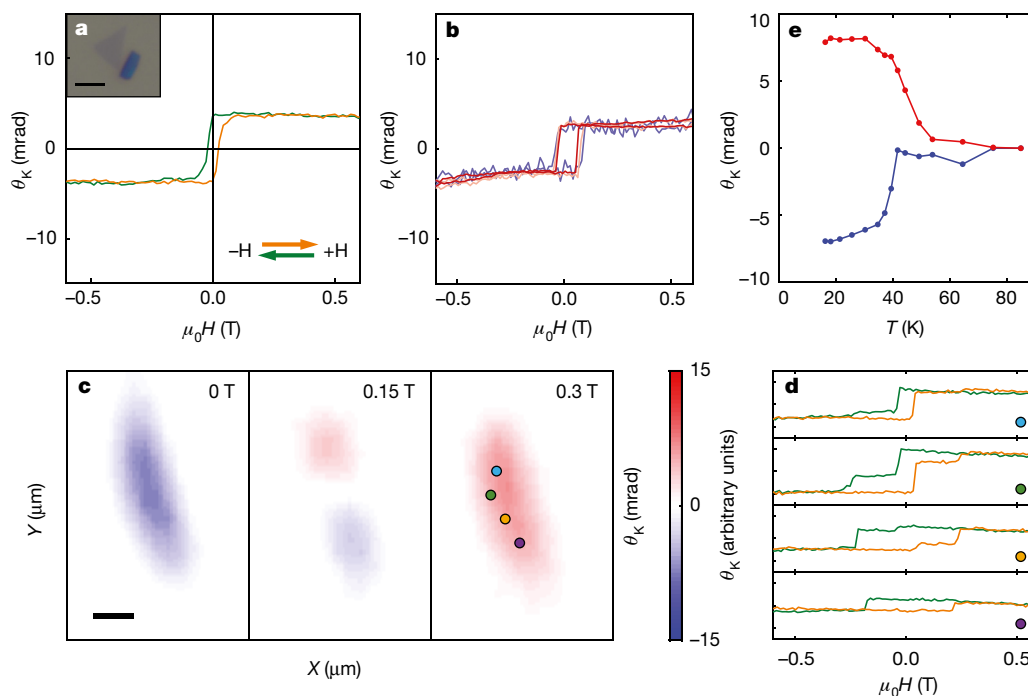


**Figure 2 | MOKE measurements of monolayer CrI<sub>3</sub>.** **a**, Polar MOKE signal for a CrI<sub>3</sub> monolayer. The inset shows an optical image of an isolated monolayer (the scale bar is 2  $\mu\text{m}$ ). **b**, Power dependence of the MOKE signal taken at incident powers of 3  $\mu\text{W}$  (blue), 10  $\mu\text{W}$  (pink), and 30  $\mu\text{W}$  (red). **c**, MOKE maps at  $\mu_0 H = 0$  T, 0.15 T and 0.3 T on a different

monolayer. The scale bar is 1  $\mu\text{m}$ . **d**,  $\theta_K$  versus  $\mu_0 H$  sweeps taken at four points marked by dots on the  $\mu_0 H = 0.3$  T map in **c**. **e**, Temperature dependence of MOKE signal with the sample initially cooled at  $\mu_0 H = 0$  T (blue) and 0.15 T (red).

blue, defined as spin down). As the field is increased to 0.15 T, the magnetization in the upper half of the flake switches direction (now spin up, in red). As the field is further increased to 0.3 T, the lower half of the monolayer flips and the entire flake becomes spin up, parallel to  $\mu_0 H$ . This observation of micrometre-scale lateral domains suggests different values of coercivity in each domain. Indeed, magnetic field sweeps ( $\theta_K$  versus  $\mu_0 H$ ) taken at discrete points ranging across both domains (Fig. 2d) show the difference in coercive field between the upper and lower half of the monolayer. Sweeps taken only on the upper domain (marked by a blue circle) show a much narrower hysteresis loop (about 50 mT) than sweeps from spots on the lower domain (orange and purple circles, about 200 mT). When the beam spot is centred between the two domains, contributions from both can be seen in the resulting hysteresis loop (green circle), a consequence of the approximately 1- $\mu\text{m}$  beam spot illuminating both domains.

To determine the monolayer  $T_C$ , we perform an analysis of the irreversible field-cooled and zero-field-cooled Kerr signal. Zero-field-cooled sweeps were performed by measuring  $\theta_K$  while cooling the sample in zero field. After warming up to a temperature well above  $T_C$  (90 K), the field-cooled measurement is taken upon cooling down in the presence of a small external magnetic field ( $\mu_0 H = 0.15$  T). Thermomagnetic irreversibility can be observed below  $T_C$ , at which point the zero-field-cooled sweep and the field-cooled sweep diverge as illustrated in Fig. 2e. We measured the average  $T_C$  for the monolayer samples to be 45 K, slightly lower than the value (61 K) for bulk samples.

The layered structure of  $\text{CrI}_3$  provides a unique opportunity to investigate ferromagnetism as a function of layer thickness. Figure 3a–c shows  $\theta_K$  versus  $\mu_0 H$  for representative 1–3-layer  $\text{CrI}_3$  samples. All measured monolayer and trilayer samples consistently show ferromagnetic behaviour with a single hysteresis loop centred at  $\mu_0 H = 0$  T (Fig. 3a and c and Extended Data Fig. 8). Both remanent and saturation values of  $\theta_K$  for trilayers are about  $50 \pm 10$  mrad, which is an order of magnitude larger than for monolayers. This drastic change in  $\theta_K$  on moving from monolayer to trilayer may be due to a layer-dependent electronic structure, leading to weaker optical resonance effects at 633 nm for the monolayer than for the trilayer (see Extended Data Fig. 9 and Methods for thin-film interference and MOKE signal in  $\text{CrI}_3$ ). We find that for trilayers and thin bulk samples,  $T_C$  is consistent with the bulk value of 61 K. The relatively small decrease of  $T_C$  from bulk to few-layer and monolayer samples suggests that interlayer interactions do not dominate the ferromagnetic ordering in  $\text{CrI}_3$ . Compared with metallic magnetic thin films whose magnetic properties strongly depend on the underlying substrate<sup>30</sup>, the weak layer-dependent  $T_C$  also implies a negligible substrate effect on the ferromagnetic phenomena in atomically thin  $\text{CrI}_3$ . As such, exfoliated  $\text{CrI}_3$  of all thicknesses can be regarded as isolated single crystals.

A further observation is that bilayer  $\text{CrI}_3$  shows a markedly different magnetic behaviour from the monolayer (Fig. 3b). For all ten bilayer samples measured, the MOKE signal is strongly suppressed, with  $\theta_K$  approaching zero (subject to slight variation between samples, see Extended Data Fig. 8b) at field values  $\pm 0.65$  T. This observation implies a compensation for the out-of-plane magnetization. Upon crossing a critical field,  $\theta_K$  shows a sharp jump, depicting a sudden recovery of the out-of-plane co-parallel orientation of the spins. This new magnetic state has a saturation  $\theta_K$  ( $40 \pm 10$  mrad) an order of magnitude larger than that of monolayer samples, and slightly smaller than for trilayers.

The suppression of the Kerr signal at zero magnetic field demonstrates that the ground state has zero out-of-plane magnetization. The plateau behaviour of the magnetization curve—showing three horizontal regimes between magnetic field values of  $-1.1$  T and  $1.1$  T (Fig. 3b)—further implies that there are no in-plane spin components; otherwise, one would expect a gradual increase of the MOKE signal with increasing perpendicular magnetic field. Rather, our observation suggests that each individual layer is ferromagnetically ordered (out-of-plane) while the interlayer coupling is antiferromagnetic. In this case, the strength of the interlayer coupling determines the field

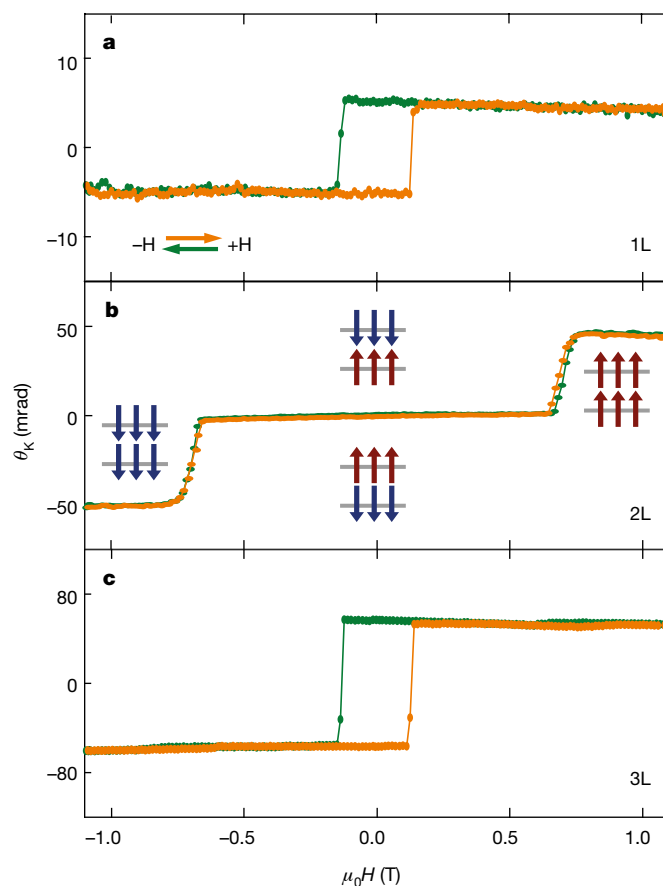


**Figure 3 | Layer-dependent magnetic ordering in atomically-thin  $\text{CrI}_3$ .** **a**, MOKE signal on a monolayer (1L)  $\text{CrI}_3$  flake, showing hysteresis in the Kerr rotation as a function of applied magnetic field, indicative of ferromagnetic behaviour. **b**, MOKE signal from a bilayer  $\text{CrI}_3$  showing vanishing Kerr rotation for applied fields  $\pm 0.65$  T, suggesting antiferromagnetic behaviour. Insets depict bilayer (2L) magnetic ground states for different applied fields. **c**, MOKE signal on a trilayer (3L) flake, showing a return to ferromagnetic behaviour.

at which jumps between different plateaus occur,  $\pm 0.65$  T. Although the detailed mechanism of this coupling remains unclear, the different magnetic phases observed in bilayers and trilayers emphasizes the strong layer-dependent interplay between different mechanisms that stabilize magnetic ordering in the atomically thin limit.

Another bilayer feature distinct from those of monolayers is the vanishingly small hysteresis around the jumps, suggesting negligible net perpendicular anisotropy. A possible interpretation is that the shape anisotropy (which prefers in-plane spin orientation) nearly compensates for the intrinsic magnetocrystalline anisotropy (which prefers out-of-plane spin orientation) so that the overall anisotropy is close to zero.

The insets in Fig. 3b display the layer-by-layer switching behaviour that leads to plausible magnetic ground states of bilayer  $\text{CrI}_3$ . When the magnetic field is  $\pm 0.65$  T, the magnetization of the two layers are oppositely oriented to one another. Thus, the net magnetization vanishes and bilayer  $\text{CrI}_3$  behaves as an antiferromagnet with an exchange field of about 0.65 T. When  $|\mu_0 H| > 0.65$  T, magnetization in one layer flips to align with the external magnetic field and restores out-of-plane magnetization, giving rise to the large MOKE signal. At around  $|\mu_0 H| = 0.65$  T, the MOKE signal sharply increases from near zero to its saturation value within about 100 mT, suggesting an abrupt increase of out-of-plane magnetization triggered by a small change of magnetic field. Such behaviour is indicative of metamagnetism, the magnetic-field-driven transition from antiferromagnetic ordering to a fully spin-polarized state<sup>20</sup>.



In summary, here we demonstrated 2D ferromagnetism in exfoliated monolayer  $\text{CrI}_3$ . The observed monolayer  $T_C$  suggests that these 2D magnets are weakly coupled to their substrates and can be regarded as isolated magnets. This is in distinct contrast with conventional metallic monolayer films, whose magnetism is strongly affected by substrate coupling. We also observed strong evidence for layer-dependent magnetic phases, from ferromagnetism in the monolayer, to antiferromagnetism in the bilayer, and back to ferromagnetism in the trilayer and bulk. We envision that the demonstration of intrinsic ferromagnetism in monolayer  $\text{CrI}_3$  as well as its layer-dependent magnetic behaviour will provide opportunities for the investigation of quantum phenomena, such as topological effects in hybrid superconducting–ferromagnetic van der Waals heterostructures as well as the engineering of new magneto-optoelectronic devices at low temperature, such as ferromagnetic light emitters.

**Online Content** Methods, along with any additional Extended Data display items and Source Data, are available in the online version of the paper; references unique to these sections appear only in the online paper.

**Received 12 January; accepted 20 April 2017.**

- Novoselov, K. S. *et al.* Electric field effect in atomically thin carbon films. *Science* **306**, 666–669 (2004).
- Xu, X., Yao, W., Xiao, D. & Heinz, T. F. Spin and pseudospins in layered transition metal dichalcogenides. *Nat. Phys.* **10**, 343–350 (2015).
- Saito, Y. *et al.* Superconductivity protected by spin-valley locking in ion-gated  $\text{MoS}_2$ . *Nat. Phys.* **12**, 144–149 (2016).
- Lu, J. M. *et al.* Evidence for two-dimensional Ising superconductivity in gated  $\text{MoS}_2$ . *Science* **350**, 1353–1357 (2015).
- Xi, X. *et al.* Ising pairing in superconducting  $\text{NbSe}_2$  atomic layers. *Nat. Phys.* **12**, 139–143 (2015).
- Tsen, A. W. *et al.* Nature of the quantum metal in a two-dimensional crystalline superconductor. *Nat. Phys.* **12**, 208–212 (2015).
- Yu, Y. *et al.* Gate-tunable phase transitions in thin flakes of 1T-TaS<sub>2</sub>. *Nat. Nanotechnol.* **10**, 270–276 (2015).
- Fei, Z. *et al.* Topological insulator behavior in monolayer  $\text{WTe}_2$ . Preprint at <https://arxiv.org/abs/1610.07924> (2016).
- Qian, X., Liu, J., Fu, L. & Li, J. Quantum spin Hall effect in two-dimensional transition metal dichalcogenides. *Science* **346**, 1344–1347 (2014).
- McGuire, M. A., Dixit, H., Cooper, V. R. & Sales, B. C. Coupling of crystal structure and magnetism in the layered, ferromagnetic insulator  $\text{CrI}_3$ . *Chem. Mater.* **27**, 612–620 (2015).
- Li, X. & Yang, J.  $\text{CrXTe}_3$  (X = Si, Ge) nanosheets: two dimensional intrinsic ferromagnetic semiconductors. *J. Mater. Chem. C* **2**, 7071–7076 (2014).
- Zhang, W.-B., Qu, Q., Zhu, P. & Lam, C.-H. Robust intrinsic ferromagnetism and half semiconductivity in stable two-dimensional single-layer chromium trihalides. *J. Mater. Chem. C* **3**, 12457–12468 (2015).
- Lin, M.-W. *et al.* Ultrathin nanosheets of  $\text{CrSiTe}_3$ : a semiconducting two-dimensional ferromagnetic material. *J. Mater. Chem. C* **4**, 315–322 (2016).
- Sivadas, N., Daniels, M. W., Swendsen, R. H., Okamoto, S. & Xiao, D. Magnetic ground state of semiconducting transition-metal trichalcogenide monolayers. *Phys. Rev. B* **91**, 235425 (2015).
- Soumyanarayanan, A., Reyren, N., Fert, A. & Panagopoulos, C. Emergent phenomena induced by spin–orbit coupling at surfaces and interfaces. *Nature* **539**, 509–517 (2016).
- Mermin, N. D. & Wagner, H. Absence of ferromagnetism or antiferromagnetism in one- or two-dimensional isotropic Heisenberg models. *Phys. Rev. Lett.* **17**, 1133–1136 (1966).
- Novoselov, K. S. *et al.* Unconventional quantum Hall effect and Berry's phase of  $2\pi$  in bilayer graphene. *Nat. Phys.* **2**, 177–180 (2006).
- Mak, K. F., Lee, C., Hone, J., Shan, J. & Heinz, T. F. Atomically thin  $\text{MoS}_2$ : a new direct-gap semiconductor. *Phys. Rev. Lett.* **105**, 136805 (2010).
- Splendiani, A. *et al.* Emerging photoluminescence in monolayer  $\text{MoS}_2$ . *Nano Lett.* **10**, 1271–1275 (2010).
- Strykowski, E. & Giordano, N. Metamagnetism. *Adv. Phys.* **26**, 487–650 (1977).
- Huang, F., Kief, M. T., Mankey, G. J. & Willis, R. F. Magnetism in the few-monolayers limit: a surface magneto-optic Kerr-effect study of the magnetic behavior of ultrathin films of Co, Ni, and Co-Ni alloys on Cu(100) and Cu(111). *Phys. Rev. B* **49**, 3962–3971 (1994).
- Back, C. H. *et al.* Experimental confirmation of universality for a phase transition in two dimensions. *Nature* **378**, 597–600 (1995).
- Elmers, H.-J., Hauschild, J. & Gradmann, U. Critical behavior of the uniaxial ferromagnetic monolayer  $\text{Fe(110)}$  on  $\text{W(110)}$ . *Phys. Rev. B* **54**, 15224–15233 (1996).
- De Jongh, L. J. & Miedema, A. R. Experiments on simple magnetic model systems. *Adv. Phys.* **50**, 947–1170 (1974).
- Carteaux, V., Moussa, F. & Spiesser, M. 2D Ising-like ferromagnetic behaviour for the lamellar  $\text{Cr}_2\text{Si}_2\text{Te}_6$  compound: a neutron scattering investigation. *Europhys. Lett.* **29**, 251 (1995).
- Sachs, B., Wehling, T. O., Novoselov, K. S., Lichtenstein, A. I. & Katsnelson, M. I. Ferromagnetic two-dimensional crystals: single layers of  $\text{K}_2\text{CuF}_4$ . *Phys. Rev. B* **88**, 201402 (2013).
- Wang, X. *et al.* Raman spectroscopy of atomically thin two-dimensional magnetic iron phosphorus trisulfide ( $\text{FePS}_3$ ) crystals. *2D Mater.* **3**, 031009 (2016).
- Tian, Y., Gray, M. J., Ji, H., Cava, R. J. & Burch, K. S. Magneto-elastic coupling in a potential ferromagnetic 2D atomic crystal. *2D Mater.* **3**, 025035 (2016).
- Dillon, J. F. Jr & Olson, C. E. Magnetization, resonance, and optical properties of the ferromagnet  $\text{CrI}_3$ . *J. Appl. Phys.* **36**, 1259 (1965).
- Sander, D. The magnetic anisotropy and spin reorientation of nanostructures and nanoscale films. *J. Phys. Condens. Matter* **16**, R603 (2004).

**Acknowledgements** Work at the University of Washington was mainly supported by the Department of Energy, Basic Energy Sciences, Materials Sciences and Engineering Division (DE-SC0008145 and SC0012509), and a University of Washington Innovation Award. Work at the Massachusetts Institute of Technology was supported by the Center for Integrated Quantum Materials under NSF grant DMR-1231319 as well as the Gordon and Betty Moore Foundation's EPiQS Initiative (grant GBMF4541 to P.J.-H.). Device fabrication was supported in part by the Center for Excitonics, an Energy Frontier Research Center funded by the US Department of Energy (DOE), Office of Science, Office of Basic Energy Sciences under Award Number DESC0001088. D.H.C.'s contribution is supported by DE-SC0002197. Work at Carnegie Mellon University is supported by DOE BES DE-SC0012509. W.Y. is supported by the Croucher Foundation (Croucher Innovation Award), the RGC of Hong Kong (HKU17305914P), and the HKU ORA. Work at Oak Ridge National Laboratory (M.A.M.) was supported by the US Department of Energy, Office of Science, Basic Energy Sciences, Materials Sciences and Engineering Division. X.X. and D.H.C. acknowledge the support of a Cottrell Scholar Award. X.X. acknowledges the support from the Clean Energy Institute (funded by the State of Washington) and from a Boeing Distinguished Professorship in Physics.

**Author Contributions** X.X. and P.J.-H. supervised the project. E.N.-M. and M.A.M. synthesized and characterized the bulk  $\text{CrI}_3$  crystal. E.N.-M. and D.R.K. fabricated the samples and analysed the layer thickness, assisted by G.C. and B.H. B.H. built the MOKE setup with help from E.S. and D.Z. G.C. and B.H. performed the MOKE measurements, assisted by K.L.S. and E.N.-M. R.C., D.X. and W.Y. provided theoretical support. B.H., G.C., E.N.-M., X.X., P.J.-H., D.X. and D.H.C. wrote the paper with input from all authors. All authors discussed the results.

**Author Information** Reprints and permissions information is available at [www.nature.com/reprints](http://www.nature.com/reprints). The authors declare no competing financial interests. Readers are welcome to comment on the online version of the paper. Publisher's note: Springer Nature remains neutral with regard to jurisdictional claims in published maps and institutional affiliations. Correspondence and requests for materials should be addressed to X.X. ([xuxd@uw.edu](mailto:xuxd@uw.edu)) and P.J.-H. ([pjarillo@mit.edu](mailto:pjarillo@mit.edu)).

## METHODS

**Growth of chromium(III) iodide bulk crystals.** Chromium powder (99.5%, Sigma-Aldrich) and anhydrous iodine beads (99.999%, Sigma-Aldrich) were mixed in a 1:3 ratio inside a glove box with an argon atmosphere. 1.5 g of the mixture was then loaded in a silica ampoule (16 mm of inner diameter, 19 mm of outer diameter and 550 mm in length). The ampoule was extracted from the glove box and immediately evacuated to a pressure of approximately  $10^{-4}$  torr. Once at that pressure, the closed end was dipped in liquid nitrogen to prevent the sublimation of the iodine beads. The ampoule was then flame-sealed under dynamic vacuum and placed inside a three-zone furnace. A three-zone furnace provides the best control over the growth process by reducing nucleation, leading to the growth of large-size single isolated crystals. Following an inverted gradient step of several hours, the crystals were grown over a period of 7 days with source zone at 650 °C (containing the solid mixture), middle growth zone at 550 °C and third zone at 600 °C. Crystals formed both in the source (lustrous hexagonal platelets of several millimetres in size) and the middle (millimetre-long ribbon-like flakes) zones. The crystals were extracted from the ampoule in an argon atmosphere and stored in anhydrous conditions. The I:Cr elemental ratio was verified to be  $2.8 \pm 0.2$  in several crystals by energy-dispersive X-ray microanalysis performed on individual crystals in a Zeiss Merlin high-resolution scanning electron microscope equipped with an electron dispersive spectroscopy probe. To confirm the crystallographic phase of the material, a few single crystals were ground, loaded into a 0.3-mm outer-diameter capillary and mounted on a Rigaku Smartlab Multipurpose Diffractometer setup in converging beam configuration with a D/teX detector. The room-temperature X-ray diffraction patterns of both the ribbon-like and hexagonal platelets were identical and consistent with the high-temperature monoclinic  $\text{AlCl}_3$ -type structure ( $C2/m$ ) reported for  $\text{CrI}_3$ , with indexed unit cell parameters of  $a = 6.8735(2)$  Å,  $b = 11.8859(3)$  Å,  $c = 6.9944(1)$  Å and  $\beta = 108.535(2)^\circ$  (Le-Bail refinement,  $R_{\text{Bragg}} = 5.27\%$ ). SQUID magnetometry performed on the single crystals depicts a  $T_C$  of 61 K and a saturation magnetization of  $3\mu_B$  per Cr atom, also in agreement with the values reported in the literature<sup>10</sup>.

**Encapsulation of samples for atomic force microscopy.**  $\text{CrI}_3$  samples exfoliated under an inert atmosphere were encapsulated to preserve the  $\text{CrI}_3$  flakes during atomic force microscopy (AFM) studies under ambient conditions. Using an all-dry viscoelastic stamping technique inside the glovebox,  $\text{CrI}_3$  flakes were sandwiched between two layers of approximately 5-nm graphite to prevent reaction with oxygen and moisture. Encapsulated  $\text{CrI}_3$  flakes could then be safely removed from the glove box for further study. AFM of graphite-encapsulated  $\text{CrI}_3$  flakes was measured using a Bruker Dimension Edge atomic force microscope in tapping mode. Extended Data Fig. 5 shows AFM results for bilayer and trilayer  $\text{CrI}_3$  flakes encapsulated in approximately 5-nm graphite layers. Their corresponding MOKE data are consistent with bare samples.

**MOKE.** Power-stabilized light from a 633-nm HeNe laser source was linearly polarized at 45° to the photoelastic modulator (PEM) slow axis (Extended Data Fig. 6)<sup>31</sup>. Transmitting through the PEM, the light was sinusoidally phase-modulated at 50.1 kHz, with a maximum retardance of  $\lambda/4$ . Upon phase modulation, the light was focused down onto the sample at normal incidence using an aspheric lens. At any point in time when the light was not circularly polarized, reflection off a magnetic sample would rotate the polarization axis (the major axis for elliptically polarized light) by what we define as the Kerr rotation,  $\theta_K$ . This reflection was then separated from the incidence path via a laser line non-polarizing beamsplitter cube and projected onto the PEM slow axis using a second polarizer. For  $\theta_K = 0$ , the slow-axis component remains constant for all polarizations and hence is not time-dependent. With a non-zero  $\theta_K$ , however, the slow-axis component depends on the polarization and oscillates at twice the modulation frequency, 100.2 kHz, with an amplitude that is proportional to the Kerr rotation. Therefore, to obtain  $\theta_K$ , the reflection was detected using an amplified photodiode and two lock-in amplifiers: one tuned at 100.2 kHz to detect the Kerr rotation, and one tuned at the chopper frequency, 800 Hz, to normalize the Kerr signal to laser intensity fluctuations and the reflectivity of the sample.

**Quantitative optical microscopy in  $\text{CrI}_3$ .** Optical microscopy images were taken using a Nikon Eclipse LV-CH 150NA optical microscope with a DS-Ri2 full-frame camera. The setup was located inside a glove box (argon atmosphere) to prevent sample degradation. The quantitative optical contrast analysis required that images were captured with a  $100\times$  objective under monochromatic illumination at normal incidence. In practice, 10-nm full-width at half-maximum (FWHM) filters were used (Andover Corp.) to filter the light coming from a halogen lamp. The thickness of the flakes was determined by contact-mode AFM under ambient conditions. Given the extreme sensitivity of the samples to atmospheric moisture, the  $\text{CrI}_3$  flakes were encapsulated between two pieces of few-layer graphite (typically 5 nm in thickness) before being extracted from the glove box. For each optical-microscopy-filtered image, individual RGB values were extracted and averaged over each flake and substrate region to give the reflected intensities of the flake

and substrate. The intensity was chosen to be exclusively the value of the channel with the highest number of counts. The experimental optical contrast value was then calculated according to the following expression (1).

$$C(d, \lambda) = \frac{I_{\text{flake}} - I_{\text{substrate}}}{I_{\text{flake}} + I_{\text{substrate}}} \quad (1)$$

Equation (1) expresses the relationship between the optical contrast  $C$  between each flake and the substrate using the reflected intensities from the flake ( $I_{\text{flake}}$ ) and the substrate ( $I_{\text{substrate}}$ ). Extended Data Fig. 1 shows an example of a contrast map of a multi-step  $\text{CrI}_3$  flake extracted from its optical micrograph.

For flakes that have been exfoliated on a  $\text{SiO}_2/\text{Si}$  substrate,  $C$  depends on the thickness of the flake and on the illumination wavelength<sup>32,33</sup>. Following the quantitative microscopy analysis proposed for graphene on  $\text{SiO}_2/\text{Si}$  substrates<sup>34</sup>,  $C$  can be computed for any kind of flake by using a model based on Fresnel's equations shown in equations (2a) and (2b):

$$I_{\text{substrate}}(\lambda) = \left| \frac{r_{02} + r_{23}e^{-2i\phi_2}}{1 + r_{02}r_{23}e^{-2i\phi_2}} \right|^2 \quad (2a)$$

$$I_{\text{flake}}(\lambda) = \left| \frac{r_{02}e^{i(\phi_1+\phi_2)} + r_{12}e^{-i(\phi_1-\phi_2)} + r_{23}e^{-i(\phi_1+\phi_2)} + r_{01}r_{12}r_{23}e^{i(\phi_1-\phi_2)}}{e^{i(\phi_1+\phi_2)} + r_{01}r_{12}e^{-i(\phi_1-\phi_2)} + r_{01}r_{23}e^{-i(\phi_1+\phi_2)} + r_{12}r_{23}e^{i(\phi_1-\phi_2)}} \right|^2 \quad (2b)$$

In this calculation, the subscripts 0, 1, 2 and 3 refer to air (treated as vacuum),  $\text{CrI}_3$ ,  $\text{SiO}_2$  and Si, respectively. The amplitude of the reflected path at the interface between media  $j$  and  $k$  is given by  $r_{jk}$  in equation (3b) and is calculated from the complex refractive indices defined in equation (3a).  $\phi_j$  is the phase shift introduced by the interaction between light of wavelength  $\lambda$  and medium  $j$  with thickness  $d_j$  shown in equation (3c).

$$\tilde{n}_j(\lambda) = n_j - i\kappa_j \quad (3a)$$

$$r_{jk} = \frac{\tilde{n}_j - \tilde{n}_k}{\tilde{n}_j + \tilde{n}_k} \quad (3b)$$

$$\phi_j = \frac{2\pi\tilde{n}_j d_j}{\lambda} \quad (3c)$$

As can be noted from the previous expressions, if one wants to model  $C$  using the Fresnel equations, the complex index of refraction of the material under study must be known. The reflectivity of  $\text{CrI}_3$  measured in vacuum at 300 K at normal incidence of a single-crystal platelet of  $\text{CrI}_3$  has been previously reported<sup>35</sup>. This data was used to calculate the phase of the amplitude reflection coefficient  $\theta$  at energies in the visible range by numerical integration, according to the Kramers–Kronig relation (4a). The refractive index  $n$  and extinction coefficient  $\kappa$  of  $\text{CrI}_3$  were then obtained throughout the visible range by combining equations (4b) and (4c) at each energy value. The results are plotted in Extended Data Fig. 3.

$$\theta(E) = -\frac{E}{\pi} \int_0^\infty \frac{\ln[R(E')]}{(E')^2 - E^2} dE' \quad (4a)$$

$$r(E) = \sqrt{R(E)} e^{i\theta(E)} \quad (4b)$$

$$r(E) = \frac{n(E) - 1 + i\kappa(E)}{n(E) + 1 + i\kappa(E)} \quad (4c)$$

Substituting for the complex indices of refraction<sup>36</sup> of  $\text{CrI}_3$ , Si and  $\text{SiO}_2$  in equations (2a) and (2b), we can calculate the expected value of  $C$  for flakes of different thicknesses as a function of the illumination wavelength. Extended Data Fig. 4a shows the contrast map for  $\text{CrI}_3$  considering a fixed thickness of 285 nm of the  $\text{SiO}_2$  layer in the  $\text{SiO}_2/\text{Si}$  substrate. We also present a line cut of that plot at an illumination wavelength of 635 nm in Extended Data Fig. 4b. It can be seen that the experimental data points closely follow the trend predicted by the model. Given that the method is non-destructive and can be performed inside a glove box for many different illumination wavelengths, the error in the determination of the number of layers can be reduced. This provides a fast and reliable method for the characterization of few-layer  $\text{CrI}_3$  flakes.

**Thin-film interferometry and the MOKE signal in  $\text{CrI}_3$ .** Linearly polarized light is an equal superposition of right-circularly and left-circularly polarized light (RCP,

LCP respectively). When a phase difference accrues between the RCP and LCP components, the polarization axis of the linearly polarized light rotates. This rotation can be observed in any material that exhibits circular birefringence. In magnetic samples, such as CrI<sub>3</sub>, this birefringence arises from a non-zero magnetization,  $\mathbf{M}$ , and is known as the magneto-optical Kerr effect (MOKE) when detected in reflection geometry. A MOKE measurement then detects changes in  $\mathbf{M}$  by exploiting the functional dependence of the Kerr rotation on the magnetization,  $\theta_K(\mathbf{M})$ . Additional interference terms must be accounted for, however, when we discuss the Kerr rotation of a thin-film material, because reflections from the material–substrate (CrI<sub>3</sub>–SiO<sub>2</sub>) interface will superimpose with the reflection off the magnetic sample (Extended Data Fig. 7). As such, this motivates a model that uses the Fresnel equations (the same formalism as in Methods subsection ‘Quantitative microscopy on CrI<sub>3</sub>’) to calculate the reflection coefficients for RCP ( $\tilde{r}_+$ ) and for LCP ( $\tilde{r}_-$ ) light. The phase difference between  $\tilde{r}_+$  and  $\tilde{r}_-$  then, is the Kerr rotation:

$$\theta_K = \arg(\tilde{r}_+) - \arg(\tilde{r}_-) \quad (5)$$

To obtain the index of refraction for CrI<sub>3</sub> when fully spin polarized, we work in Cartesian coordinates and use a dielectric tensor of the form<sup>37</sup>:

$$\epsilon = \begin{bmatrix} \tilde{\epsilon}_{xx} & iQM & 0 \\ -iQM & \tilde{\epsilon}_{xx} & 0 \\ 0 & 0 & \tilde{\epsilon}_{zz} \end{bmatrix} \quad (6)$$

where  $Q$  is the complex Voigt constant and  $M$  is the out-of-plane (parallel to the  $z$ -axis) component of the magnetization, which we assume is constant for all CrI<sub>3</sub> thicknesses when fully spin-polarized. This form of the dielectric tensor for a magnetic sample is valid assuming (1) that the crystal exhibits at least threefold symmetry; (2) that  $\mathbf{M}$  is parallel to the axis of rotation that gives rise to the threefold symmetry; and (3) that the axis of rotation is chosen to be the  $z$  axis. Solving for the normal modes, we obtain the eigenvalues:

$$\tilde{n}_{\pm} = \sqrt{\tilde{\epsilon}_{xx} \pm QM} \quad (7)$$

and the eigenvectors:

$$\mathbf{D}_{\pm} = (E_x \pm iE_y)\hat{\mathbf{z}} \quad (8)$$

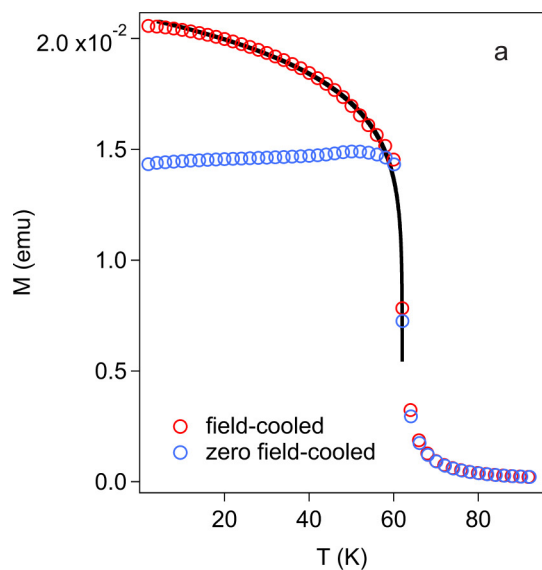
where  $\tilde{n}_+$  and  $\mathbf{D}_+$  denote the eigenvalue and eigenvector respectively of RCP light and  $\tilde{n}_-$  and  $\mathbf{D}_-$  denote the eigenvalue and eigenvector respectively of LCP light in CrI<sub>3</sub>. The complex dielectric component  $\tilde{\epsilon}_{xx}$ , when related to the  $\tilde{n}$  defined in equation (3a), is:

$$\tilde{\epsilon}_{xx} = n^2 - \kappa^2 - 2in\kappa \quad (9)$$

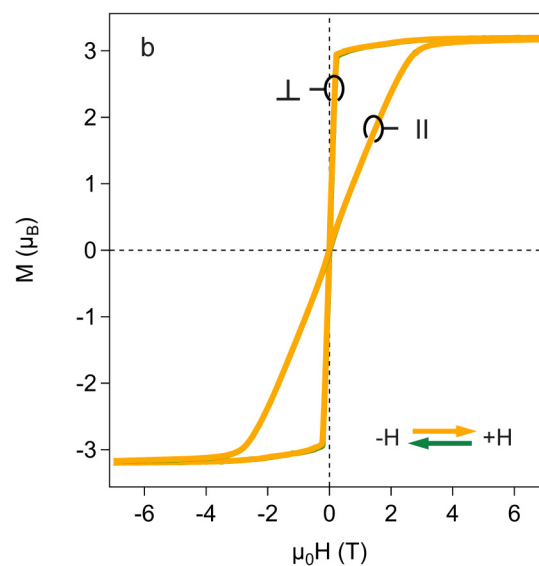
where the value of  $\tilde{\epsilon}_{xx}$  was derived from the  $n$  and  $\kappa$  values at about 1.96 eV (modelled in Extended Data Fig. 3). It is apparent from equation (7) that we should not expect  $\theta_K$  to depend linearly on  $\mathbf{M}$  and layer number. In addition, interference from reflections off the CrI<sub>3</sub>–SiO<sub>2</sub> interface will give rise to a non-trivial functional form of  $\theta_K$  with respect to layer thickness. There is no determination of  $Q$  in the literature for CrI<sub>3</sub>, so we varied  $Q$  as a complex parameter and constrained it to a small range that fitted experimental  $\theta_K$  values from our MOKE measurements on trilayer and bulk CrI<sub>3</sub>. These calculations qualitatively describe the large increase in  $\theta_K$  moving from monolayer to trilayer, as well as the negative  $\theta_K$  seen at positive  $\mu_0 H$  for bulk flakes. However, this simple model does not incorporate layer-dependent electronic structure changes, seen in other atomically thin van der Waals materials such as<sup>18</sup> MoS<sub>2</sub>, and evident in this system as a change in magnetic ground states from monolayer to bilayer.

**Data availability.** The data sets generated during and analysed during this study are available from the corresponding author upon reasonable request.

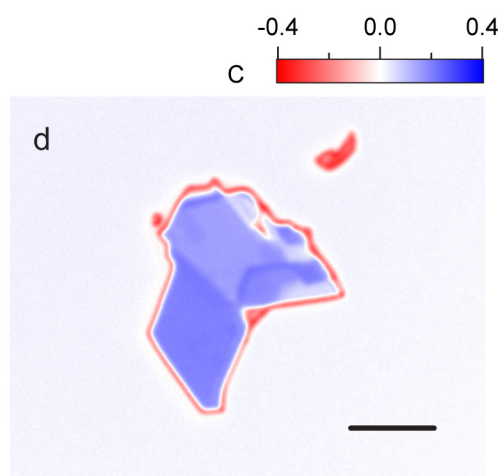
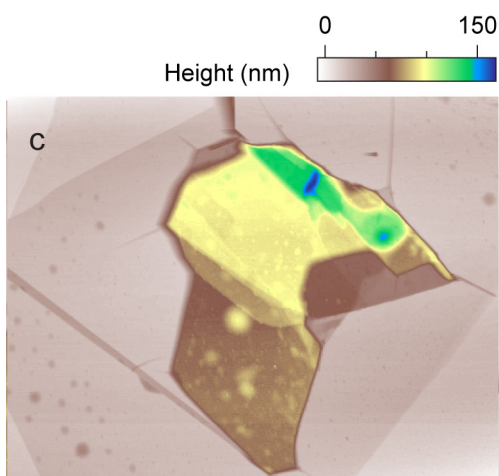
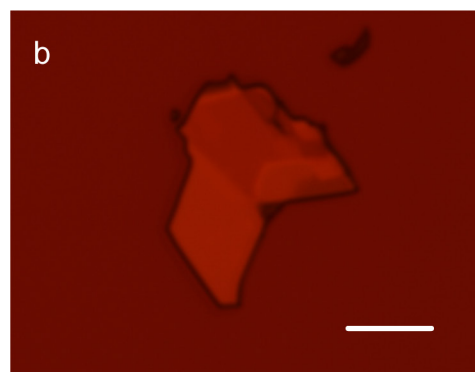
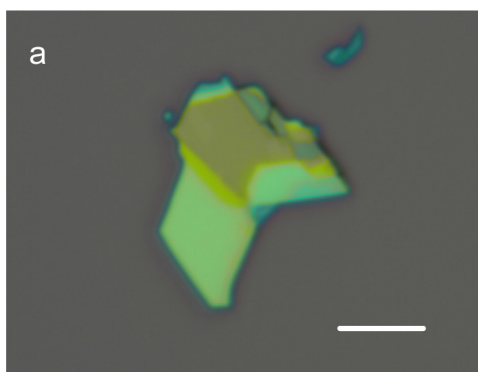
31. Katsuaki, S. Measurement of magneto-optical Kerr effect using piezo-birefringent modulator. *Jpn. J. Appl. Phys.* **20**, 2403 (1981).
32. Beal, A. R., Hughes, H. P. & Liang, W. Y. The reflectivity spectra of some group VA transition metal dichalcogenides. *J. Phys. C* **8**, 4236 (1975).
33. Castellanos-Gomez, A. *et al.* Fast and reliable identification of atomically thin layers of TaSe<sub>2</sub> crystals. *Nano Res.* **6**, 191–199 (2013).
34. Blake, P. *et al.* Making graphene visible. *Appl. Phys. Lett.* **91**, 063124 (2007).
35. Grant, P. M. & Street, G. B. Optical properties of chromium trihalides in the region 1–11 eV. *Bull. Am. Phys. Soc. II* **13**, 3 (1968).
36. Herzinger, C. *et al.* Ellipsometric determination of optical constants for silicon and thermally grown silicon dioxide via a multi-sample, multi-wavelength, multi-angle investigation. *J. Appl. Phys.* **83**, 3323 (1998).
37. Ebert, H. Magneto-optical effects in transition metal systems. *Rep. Prog. Phys.* **59**, 1665–1735 (1996).



**Extended Data Figure 1 | SQUID magnetometry in bulk CrI<sub>3</sub>.** **a**, Zero-field-cooled/field-cooled temperature dependence of the magnetization of a CrI<sub>3</sub> bulk crystal with an applied magnetic field of 10 G perpendicular to the basal plane of the sample. The black line is a criticality fit



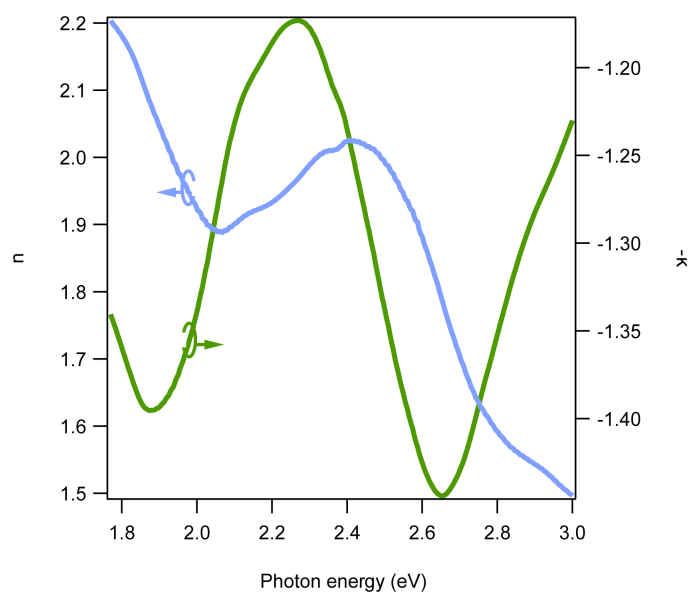
( $M = \alpha(1 - T_C/T)^\beta$ ) of the data with  $T_C = 61$  K and  $\beta = 0.125$  (Ising universality class). **b**, Hysteresis loops of the same sample with the external magnetic field in perpendicular and parallel orientations with respect to the CrI<sub>3</sub> layers. (emu, electromagnetic units.)



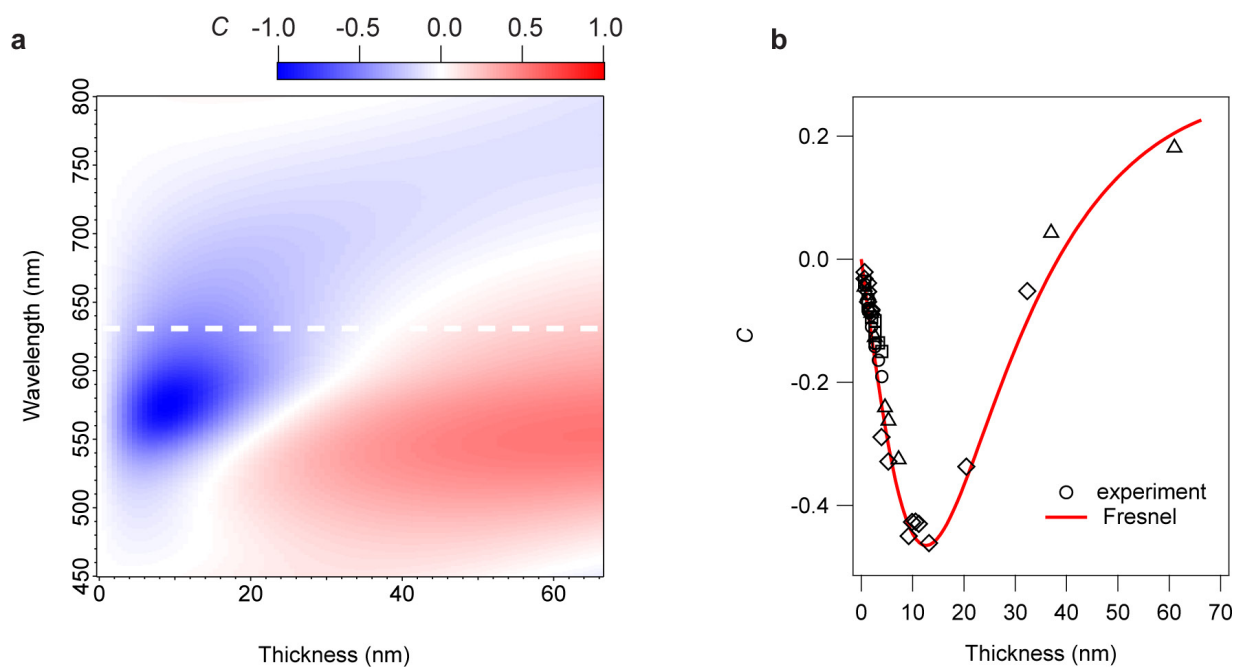
**Extended Data Figure 2 | Thickness dependence of the optical contrast of the  $\text{CrI}_3$  flakes.** Optical micrographs of a  $\text{CrI}_3$  flake illuminated with white light (**a**) and with 631-nm-(10-nm FWHM bandpass)-filtered light (**b**).

**c**, AFM topography image of the same sample. **d**, Optical contrast map extracted from the 631-nm micrograph in **b**. Scale bars are 5  $\mu\text{m}$ .



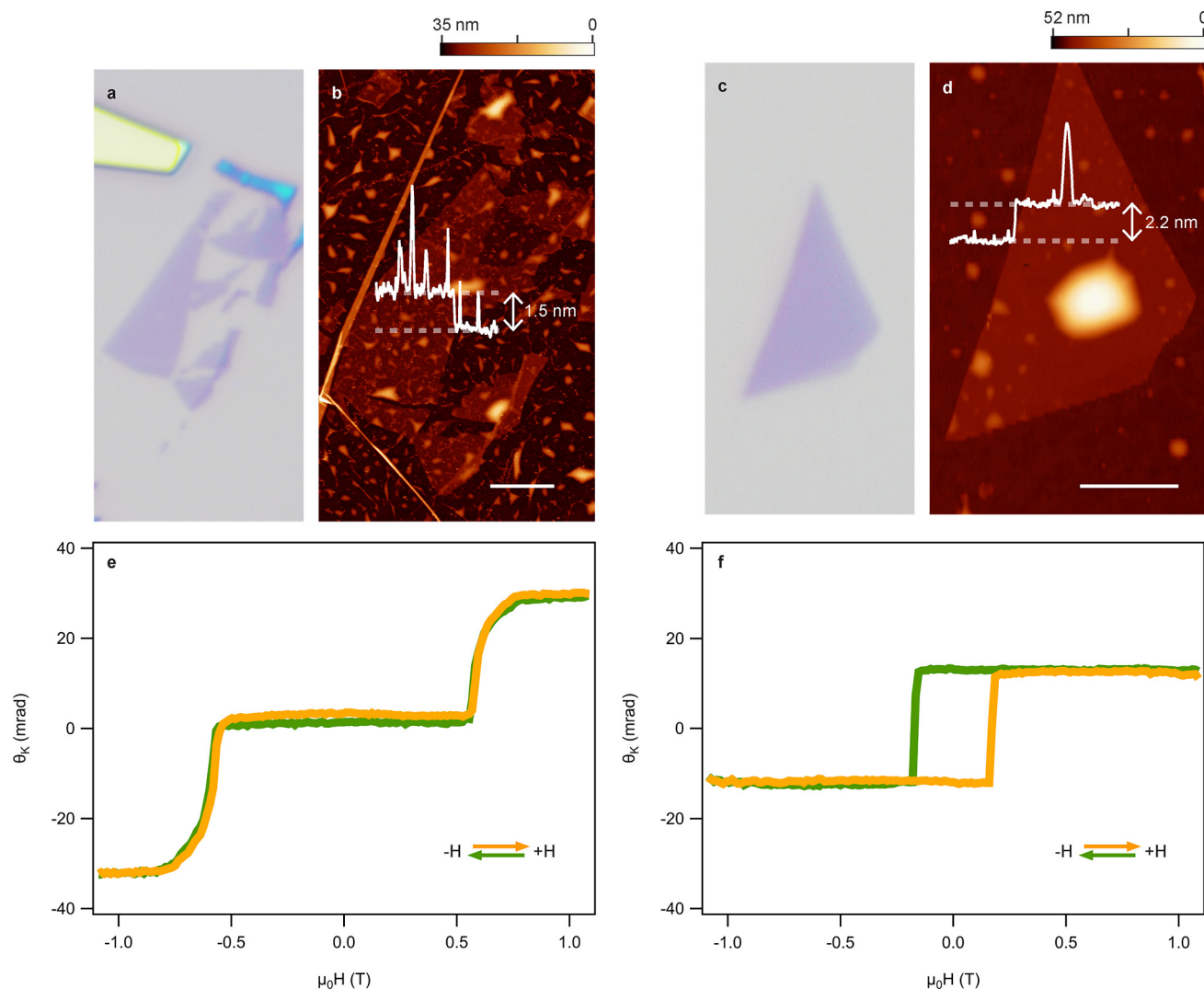


**Extended Data Figure 3 | Computed index of refraction of bulk  $\text{CrI}_3$ .** Real ( $n$ ) and imaginary ( $\kappa$ ) components are plotted as a function of photon energy in the visible range.



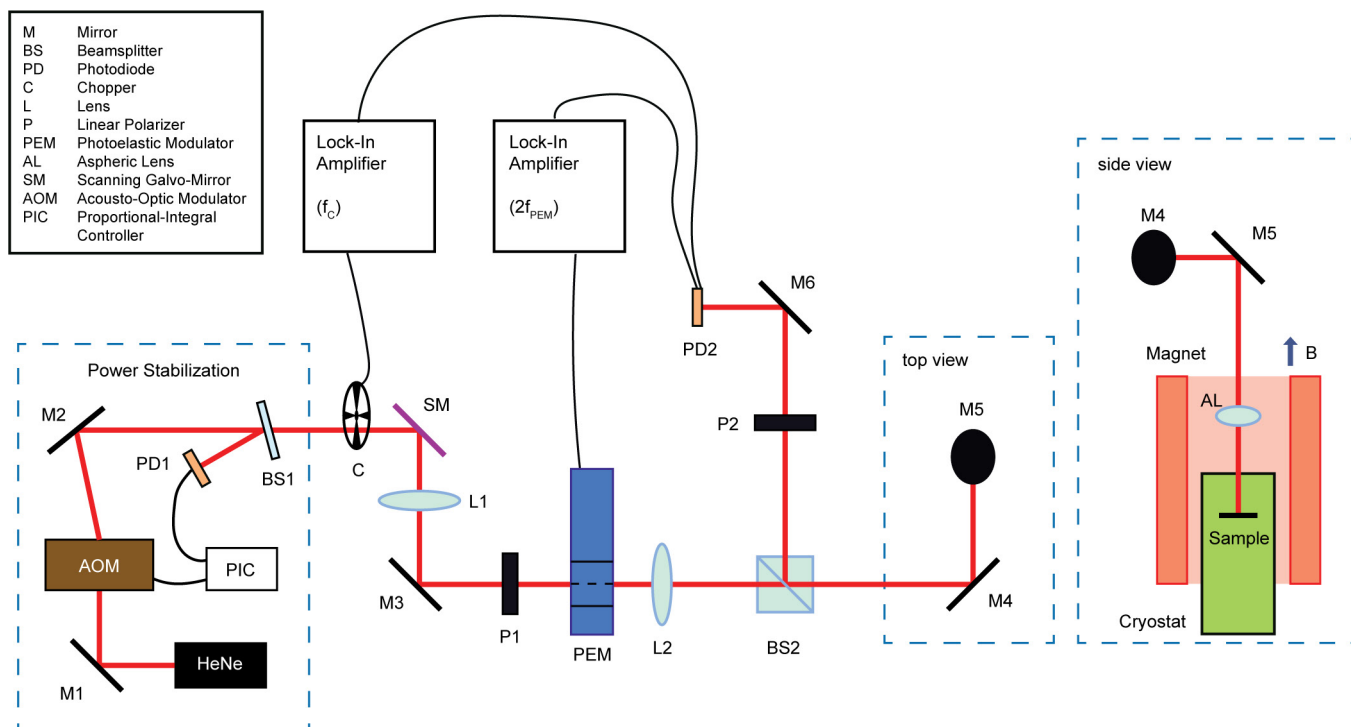
**Extended Data Figure 4 | Fresnel model for the optical contrast  $C$  of  $\text{CrI}_3$  flakes on  $\text{Si}/285\text{ nm SiO}_2$  substrates. **a**, Dependence of  $C$  with the number of layers for a  $\text{CrI}_3$  flake as a function of the illumination wavelength. **b**, Comparison of the experimental data with the computed**

thickness dependence of  $C$  for a red-light-illuminated sample (line cut at 631 nm as shown by the dashed line in **a**). The different shape markers indicate data coming from different exfoliated samples.



**Extended Data Figure 5 | AFM and MOKE measurements of graphite-encapsulated few-layer  $\text{CrI}_3$ .** **a**, Optical microscope image of a bilayer  $\text{CrI}_3$  flake on 285-nm-thick  $\text{SiO}_2$ . **b**, AFM data for the  $\text{CrI}_3$  flake in **a** encapsulated in graphite, showing a line cut across the flake with a step height of 1.5 nm. **c**, Optical microscope image of a trilayer  $\text{CrI}_3$

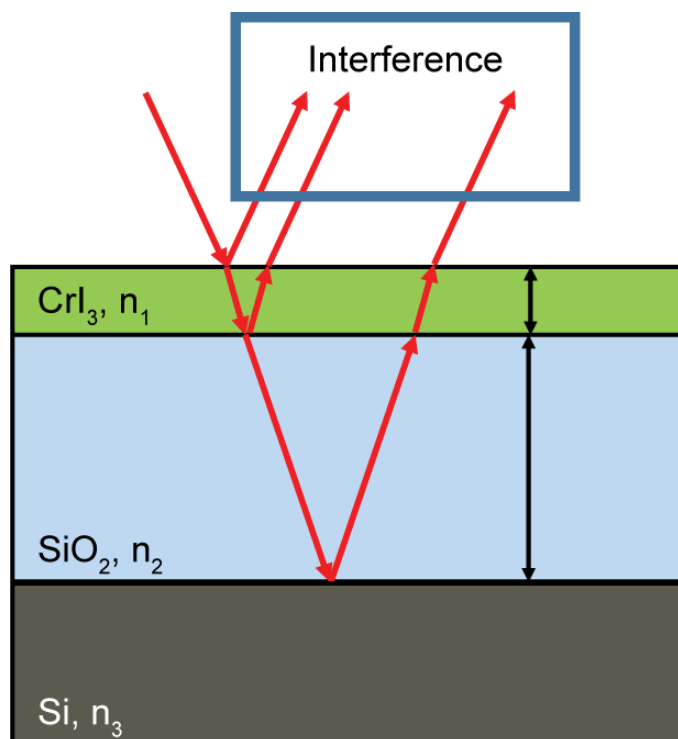
flake on 285-nm-thick  $\text{SiO}_2$ . **d**, AFM data for the  $\text{CrI}_3$  flake shown in **c** encapsulated in graphite. A line cut taken across the flake shows a step height of 2.2 nm. Both scale bars are 2  $\mu\text{m}$ . **e** and **f** show the MOKE signal as a function of applied magnetic field for the encapsulated bilayer in **b** and the encapsulated trilayer in **d** respectively.



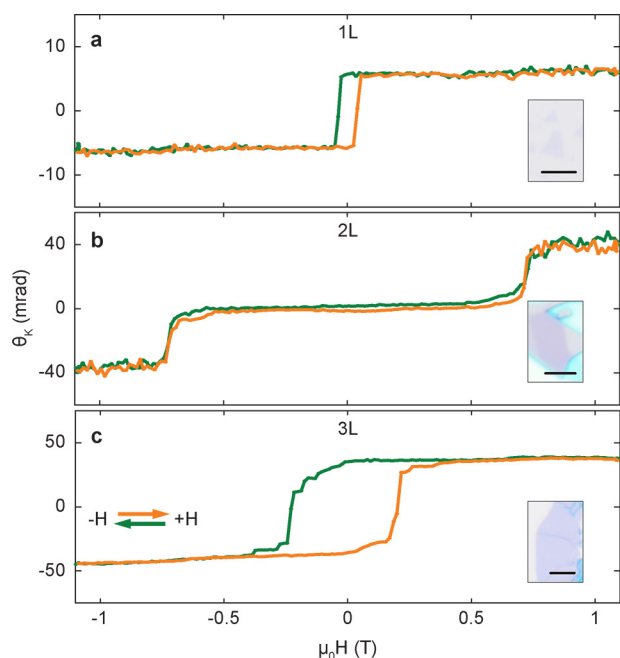
**Extended Data Figure 6 | Magneto-optical Kerr effect experimental setup.** Schematic of the optical setup used to measure the MOKE effect in  $\text{CrI}_3$  samples. 633 nm optical excitation is provided by a power-stabilized HeNe laser. A mechanical chopper and photoelastic modulator provide intensity and polarization modulation, respectively. The modulated beam is directed through a polarizing beam splitter to the sample, housed in

a closed-cycle cryostat at 15 K. A magnetic field is applied at the sample using a 7-T solenoidal superconducting magnet in Faraday geometry. The reflected beam passes through an analyser onto a photodiode, where lock-in detection measures the reflected intensity (at  $f_C$ ) as well as the Kerr rotation (at  $f_{\text{PEM}}$ ).

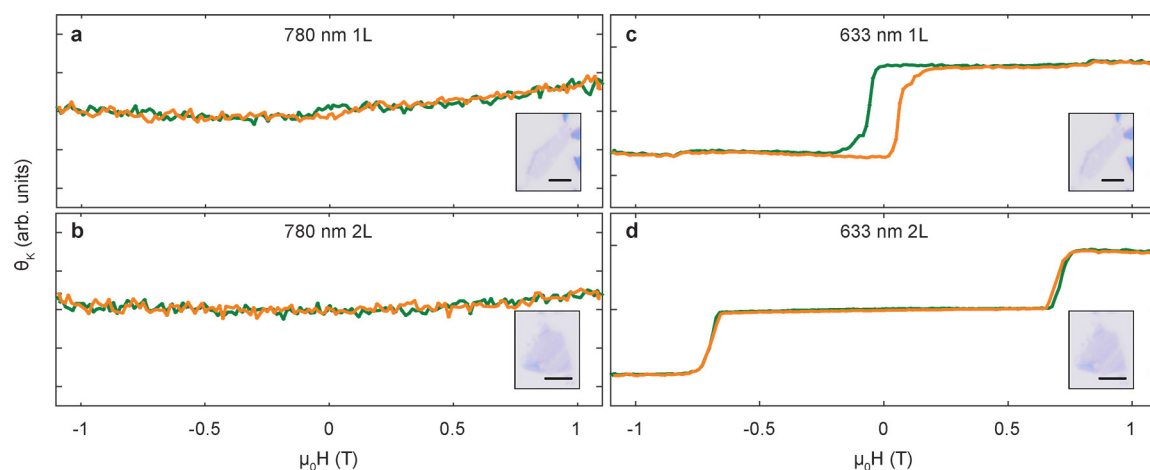




**Extended Data Figure 7 | Thin-film interference ray diagram of  $\text{CrI}_3$  on a silicon oxide/silicon substrate.** Light incident on  $\text{CrI}_3$  undergoes reflections at the  $\text{CrI}_3$ – $\text{SiO}_2$  interface (green–blue boundary) as well as the  $\text{SiO}_2$ – $\text{Si}$  interface (blue–grey boundary). These reflections interfere with the initial reflection off the  $\text{CrI}_3$  flake to produce thin-film interference that depends on the  $\text{CrI}_3$  layer thickness,  $d_1$ , as well as the  $\text{SiO}_2$  thickness,  $d_2$ . The underlying silicon wafer is assumed to be semi-infinite. The indices of refraction for  $\text{CrI}_3$ ,  $\text{SiO}_2$ , and  $\text{Si}$  are  $n_1$ ,  $n_2$  and  $n_3$  respectively.



**Extended Data Figure 8 | Additional data for 1–3-layer samples showing Kerr rotation as a function of the applied magnetic field.** The insets show optical microscope images of the CrI<sub>3</sub> flakes at 100 $\times$  magnification. **a**, Additional monolayer data showing ferromagnetic hysteresis and remanent Kerr signal as a function of applied magnetic field. **b**, Additional bilayer data showing field-dependent behaviour consistent with an antiferromagnetic ground state. **c**, Additional trilayer data showing field-dependent behaviour consistent with a ferromagnetic ground state, as well as a larger remanent Kerr signal than the monolayer in **a**. All scale bars are 5  $\mu$ m.



**Extended Data Figure 9 | Additional data for monolayer and bilayer samples under 780-nm excitation and 633-nm excitation.** Insets show optical microscope images of the CrI<sub>3</sub> flakes at 100 $\times$  magnification.

**a**, Kerr rotation as a function of applied magnetic field for a monolayer **a** (or **c**), and a bilayer **b** (or **d**) under 780-nm (or 633-nm) excitation. All scale bars are 4  $\mu$ m.